Performing the full angular analysis of $\overline{B}_d \to \overline{K}^{*0}\mu^+\mu^-$ at LHC*b*

William Reece* and Ulrik Egede†

Imperial College London

$\overline{B}_d \to \overline{K}^{*0}\mu^+\mu^-$ is a rare electroweak $b \to s$ penguin decay that is thought to have excellent sensitivity to physics beyond the Standard Model. In this note we present a general method for performing the full angular analysis of the decay which gives access to a set of observables which are very sensitive to non–Standard Model right–handed currents. The experimental sensitivity to these observables for 2, 10 and 100 fb^{-1} of LHC*b* data is presented. Where possible, these are compared to a previously investigated method based on angular projections.

I. INTRODUCTION

The search for physics beyond the Standard Model (SM) was one of the primary motivations for the construction of LHC*b*. There are two common approaches for these searches; direct and indirect. LHC*b* is well suited to the indirect approach where the SM prediction for a given B decay is compared with experimental observations. Effective field theory techniques can be used to make this comparison in a model independent way so that only general classes of new physics (NP) need to be studied (see Sec. II) but considerable precision is required from both theory and experiment. LHC*b* should provide an excellent laboratory for conducting these kind of searches and could play a key role in discriminating between different NP models.

In recent years, interest in $b \to s$ quark transitions has increased. The lack of flavor changing neutral currents in the SM means that these transitions must occur via a loop diagram. Decays which proceed in this way may be sensitive to many classes of NP as, in addition to the SM particles, new heavy degrees of freedom can contribute to the amplitudes in a relatively unconstrained way. Despite the success of the B–factories, experimental limits

*w.reece06@imperial.ac.uk

†u.egede@imperial.ac.uk

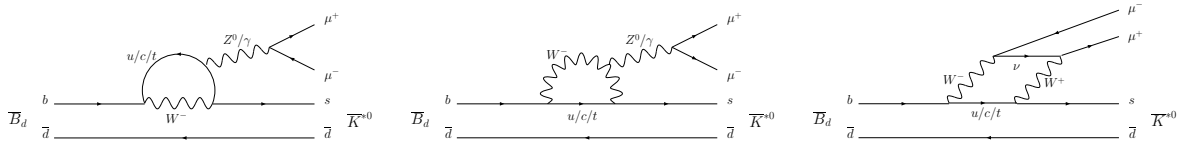

(a) Quark Penguin (b) W Penguin (c) W Box

FIG. 1: SM Feynman diagrams for the $\overline{B}_d \to \overline{K}^{*0}\mu^+\mu^-$ decay.

are currently modest and there are theoretical reasons to think that there may be non–SM effects present (for a review see [1]). In this note, the technical details for performing a full angular analysis will be discussed for the rare $b \to s$ decay $\overline{B}_d \to \overline{K}^{*0}\mu^+\mu^-$. A set of angular observables with sensitivity to some classes of NP will be extracted. A more theoretical review of these observables is given in Ref. [2].

The rest of this note is laid out as follows. In the next section we introduce the decay from a theoretical standpoint and then review some of the observables to be measured. In Sec. III we give details of a toy Monte–Carlo model of the decay which is then used to extract sensitivities to the angular observables at LHCb using a full angular analysis. In Sec. V we review previous work on extracting some of these angular observables and compare the results obtained, while in Sec. VI we explore how much model discrimination LHCb could provide if nature indeed has enhanced right–handed currents. Finally in Sec. VII we summarise our findings and give some outlook for the future.

II. $\overline{B}_d \to \overline{K}^{*0}\mu^+\mu^-$

$\overline{B}_d \to \overline{K}^{*0}\mu^+\mu^-$ [1] is a flavour changing neutral current (FCNC) $b \to s$ decay that proceeds via penguin and box diagrams such as those shown in Fig. 1. It was first observed at Belle [3] and has a branching ratio of $(1.10^{+\ 0.29}_{-\ 0.26}) \times 10^{-6}$ [4]. The decay is sensitive to NP contributions through the addition of new diagrams where charged or neutral NP particles run in the loop [5–8]. Studies show that the decay can be selected at LHCb, giving approximately 4000 signal and 1000 signal–like background events in the range $4m_\mu^2 \leq q^2 \leq$

[1] In this note we deal with the $\overline{B}_d$ as this contains the b quark. The formalism can be applied equally to the B_d with appropriate redefinitions which will be indicated explicitly in the text.

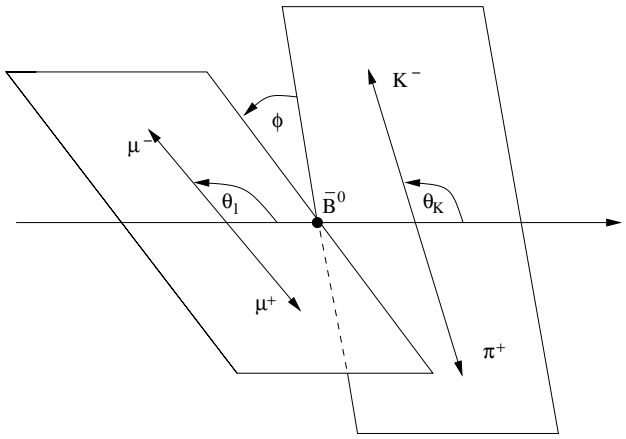

FIG. 2: The angles used to describe the decay $\overline{B}_d \to \overline{K}^{*0}\mu^+\mu^-$. θ_L is the angle between the μ^- and the $\overline{B}_d$ in the $\mu^+\mu^-$ rest frame. θ_K is the angle between the K^- in the $\overline{K}^*$ rest frame, and ϕ is the angle between the $\mu^+\mu^-$ and $\overline{K}^*$ decay planes. For the B_d, the angles are measured relative to the μ^+ and K^+.

$9\,\mathrm{GeV}^2/c^4$ per $2\,\mathrm{fb}^{-1}$ [9], which corresponds to one nominal year of stable data–taking. Both *BABAR* and Belle have published tantalising results for the decay [10–14] and the vastly increased yields expected at LHCb will allow significant improvement on these.

A. Angular Distribution

We assume that the $\overline{K}^{*0}$ always decays on its mass shell to a K^- and a π^+, explicitly ignoring any non–resonant $\overline{B}_d \to K^-\pi^+\mu^+\mu^-$ contributions[2]. In this approximation, the decay is completely kinematically constrained by three decay angles, θ_L, θ_K, and ϕ, and by the invariant mass of the muon pair, q^2. The angles are defined in the intervals

$$0 \le \theta_l \le \pi\,, \quad 0 \le \theta_K \le \pi\,, \quad -\pi \le \phi < \pi\,, \tag{1}$$

where only the ϕ angle is signed. The decay kinematics are shown in Fig. 2 and the definitions of the angles are given in the caption. We work in the massless lepton approximation and avoid consideration of the q^2 region below $1\,\mathrm{GeV}^2/c^4$. In this case, we can derive a simplified

[2] The size of these non–resonant contributions is currently unknown, but expected to be small. These contributions will affect the angular distribution, as it no–longer fully Pseudoscalar→ VectorVector, but may give additional NP sensitivity [15].

differential decay width for the $\overline{B}_d$, where a sum over final state particle spins has been included. The distribution for the $\overline{B}_d$ is

$$\frac{d^4\Gamma_{\overline{B}_d}}{dq^2\, d\theta_l\, d\theta_K\, d\phi} = \frac{9}{32\pi} I(q^2, \theta_l, \theta_K, \phi) \sin\theta_l \sin\theta_K \,, \tag{2}$$

where the physical region of phase space is $4m_l^2 \leq q^2 \leq (m_B - m_{K^*})^2$ and

$$\begin{aligned} I \;=\; & I_1 + I_2 \cos 2\theta_l + I_3 \sin^2\theta_l \cos 2\phi + I_4 \sin 2\theta_l \cos\phi + I_5 \sin\theta_l \cos\phi + I_6 \cos\theta_l \\ +\; & I_7 \sin\theta_l \sin\phi + I_8 \sin 2\theta_l \sin\phi + I_9 \sin^2\theta_l \sin 2\phi. \end{aligned} \tag{3}$$

For the B_d

$$\frac{d^4\Gamma_{B_d}}{dq^2\, d\theta_l\, d\theta_K\, d\phi} = \frac{9}{32\pi} \overline{I}(q^2, \theta_l, \theta_K, \phi) \sin\theta_l \sin\theta_k \,, \tag{4}$$

and if CP conservation is assumed, we have

$$I_{1,2,3,4,6,7} \;=\; \overline{I}_{1,2,3,4,6,7} \,, \tag{5a}$$

$$I_{5,8,9} \;=\; -\overline{I}_{5,8,9} \,. \tag{5b}$$

The functions I_{1-9} in Eq. (3) can be written in terms of the K^{*0} spin amplitudes A_t, A_0, $A_\parallel$, $A_\perp$; the later three have both left– and right–handed components and all are functions of q^2. A_t corresponds to the scalar component of the virtual $\overline{K}^{*0}$, which is negligible if the lepton mass is small in comparison to the mass of the lepton pair. For $m_l = 0$, we find,

$$I_1 \;=\; \frac{3}{4}\left(|A_{\perp L}|^2 + |A_{\parallel L}|^2 + (L \to R)\right)\sin^2\theta_K + \left(|A_{0L}|^2 + |A_{0R}|^2\right)\cos^2\theta_K, \tag{6a}$$

$$I_2 \;=\; \frac{1}{4}(|A_{\perp L}|^2 + |A_{\parallel L}|^2)\sin^2\theta_K - |A_{0L}|^2\cos^2\theta_K + (L \to R), \tag{6b}$$

$$I_3 \;=\; \frac{1}{2}\Big[(|A_{\perp L}|^2 - |A_{\parallel L}|^2)\sin^2\theta_K + (L \to R)\Big], \tag{6c}$$

$$I_4 \;=\; \frac{1}{\sqrt{2}}\Big[\mathrm{Re}(A_{0L}A^*_{\parallel L})\sin 2\theta_K + (L \to R)\Big], \tag{6d}$$

$$I_5 \;=\; \sqrt{2}\Big[\mathrm{Re}(A_{0L}A^*_{\perp L})\sin 2\theta_K - (L \to R)\Big], \tag{6e}$$

$$I_6 \;=\; 2\Big[\mathrm{Re}(A_{\parallel L}A^*_{\perp L})\sin^2\theta_K - (L \to R)\Big], \tag{6f}$$

$$I_7 \;=\; \sqrt{2}\Big[\mathrm{Im}(A_{0L}A^*_{\parallel L})\sin 2\theta_K - (L \to R)\Big], \tag{6g}$$

$$I_8 \;=\; \frac{1}{\sqrt{2}}\Big[\mathrm{Im}(A_{0L}A^*_{\perp L})\sin 2\theta_K + (L \to R)\Big], \tag{6h}$$

$$I_9 \;=\; \Big[\mathrm{Im}(A^*_{\parallel L}A_{\perp L})\sin^2\theta_K + (L \to R)\Big]. \tag{6i}$$

The $(L \to R)$ terms above represent a repeat of the previous terms with the left–handed amplitudes exchanged for right–handed. It is by extracting the values of these amplitudes that we can detect the effects of physics beyond the SM.

B. Symmetries

The angular distribution has three independent global symmetries in the $m_l = 0$ limit. In this case there is no interference between right– and left–handed amplitudes so the distribution is invariant under both L and R global phase transformations,

$$A^{'}_{\perp L} = e^{i\phi_L} A_{\perp L},\ A^{'}_{\parallel L} = e^{i\phi_L} A_{\parallel L},\ A^{'}_{0L} = e^{i\phi_L} A_{0L} \tag{7}$$

and

$$A^{'}_{\perp R} = e^{i\phi_R} A_{\perp R},\ A^{'}_{\parallel R} = e^{i\phi_R} A_{\parallel R},\ A^{'}_{0R} = e^{i\phi_R} A_{0R}\ . \tag{8}$$

There is also an additional global symmetry under continuous $L \leftrightarrow R$ rotations,

$$A^{'}_{\perp L} = +\cos\theta A_{\perp L} - \sin\theta A^{*}_{\perp R} \tag{9a}$$

$$A^{'}_{\perp R} = +\sin\theta A_{\perp L} + \cos\theta A^{*}_{\perp R} \tag{9b}$$

$$A^{'}_{0L} = +\cos\theta A_{0L} - \sin\theta A^{*}_{0R} \tag{9c}$$

$$A^{'}_{0R} = +\sin\theta A_{0L} + \cos\theta A^{*}_{0R} \tag{9d}$$

$$A^{'}_{\parallel L} = +\cos\theta A_{\parallel L} + \sin\theta A^{*}_{\parallel R} \tag{9e}$$

$$A^{'}_{\parallel R} = -\sin\theta A_{\parallel L} + \cos\theta A^{*}_{\parallel R}\ . \tag{9f}$$

These relations must be taken into account when constructing both angular observables and the full angular fit.

C. Angular Observables

Looking for NP through indirect methods is complementary to direct searches. Central to the indirect method is the operator product expansion (OPE). This allows interactions to be parameterised through an effective theory made up of effective couplings and their associated coupling constants, known as the Wilson coefficients. For $b \to s$ transitions the decay amplitude can be written in terms of an effective Hamiltonian,

$$\mathcal{H}_{eff} = -\frac{4G_{\rm F}}{\sqrt{2}} V_{\rm tb} V^{*}_{\rm ts} \sum_i \left[C_i(\mu)\mathcal{O}_i(\mu) + C^{\prime}_i(\mu)\mathcal{O}^{\prime}_i(\mu) \right], \tag{10}$$

where $V_{\rm tb}$ and $V_{\rm ts}$ are the relevant CKM factors and primes (no primes) denote right–handed (left–handed) contributions. The local operators $\mathcal{O}_i(\mu)$ describe the long–range contributions to the decay, while the short–range contributions, coming from integrated out heavy degrees of freedom, are parameterised by the Wilson coefficients $C_i(\mu)$.

$\overline{B}_d \to \overline{K}^{*0}\mu^+\mu^-$ is dominated by the operators $\mathcal{O}_{7,9,10}$, definitions of which can be found in Ref. [16]. $\mathcal{O}_7^{(\prime)}$ dominates the low q^2 region while $\mathcal{O}_{9,10}^{(\prime)}$ are more important at higher q^2. The presence of new and unaccounted for heavy degrees of freedom will shift the values of the corresponding Wilson coefficients away from their SM values. Additional NP effects can be included by introducing non–SM operators, for example parameterising possible scalar or pseudo–scalar contributions [17, 18]. By measuring the values of the Wilson coefficients we can make a model independent test of the SM, and also powerfully exclude general classes of NP models.

We are interested in extracting information about NP from the measured angular distribution in the decay. This can be done in several ways:

- The angular distribution can be expressed in terms of the Wilson coefficients and a fit made to the observed distribution. Due to the large uncertainty in the form factors introduced by pQCD this approach would leave us with a large theoretical uncertainty on the extracted Wilson coefficients.

- For a set of NP models one could compute the full angular distribution and compare it to the observed angular distribution. On a *model–by–model* basis it would then be possible to exclude them as being incompatible with the observations. This approach is obviously not model independent and would make it very difficult to use the quoted results to exclude models that were not considered at the time of publication.

- One can derive a set of observables which can be extracted directly from the observed angular distribution but at the same time have the advantage that theoretical uncertainties cancel out. In this way you retain the model independence and also reduce the theoretical uncertainty in the quoted results. For any new theory these new observables can be calculated at a later date.

We have chosen the last of these approaches. The observables are carefully constructed combinations of the spin amplitudes, which are themselves functions of the Wilson coefficients.

We need to find observables with good sensitivity to any NP operators, small theoretical uncertainties and finally good experimental resolutions. We refer the interested reader to Ref. [2] for more details.

The main source of theoretical uncertainty comes from the form factors that parameterise the $\overline{B}_d \to \overline{K}^{*0}$ transition and also enter into the spin amplitudes. These are dominated by long–range effects and have to be treated non–perturbatively using approximate methods [5]. At leading order (LO), the seven *a priori* independent form factors reduce to two universal 'soft' form factors[3], $\zeta_{||}$ and $\zeta_{\perp}$ [19–22], valid in the range $1 \leq q^2 \leq 6\,\mathrm{GeV}^2/c^4$. These can then be used to form observables where the universal form factors cancel out, much reducing the overall theoretical uncertainty (see for example [16]). Outside of the $1 \leq q^2 \leq 6\,\mathrm{GeV}^2/c^4$ range these cancellations cannot be made, leading to much greater theoretical uncertainties on the observables. In this note, only the theoretically clean q^2 region specified above will be considered.

The angular observables to be investigated are:

$$A_{\mathrm{FB}} = \frac{3}{2}\frac{\mathrm{Re}(A_{\|L}A^*_{\perp L}) - \mathrm{Re}(A_{\|R}A^*_{\perp R})}{\Gamma'}, \tag{11}$$

$$A_{\mathrm{Im}} = \frac{\mathrm{Im}(A_{\perp L}A^*_{\|L}) + \mathrm{Im}(A_{\perp R}A^*_{\|R})}{\Gamma'}, \tag{12}$$

$$A_T^{(2)} = \frac{|A_{\perp}|^2 - |A_{\|}|^2}{|A_{\perp}|^2 + |A_{\|}|^2}, \tag{13}$$

$$A_T^{(3)} = \frac{|A_{0L}A^*_{\|L} - A^*_{0R}A_{\|R}|}{\sqrt{|A_0|^2 \times |A_{\perp}|^2}}, \tag{14}$$

$$A_T^{(4)} = \frac{|A_{0L}A^*_{\perp L} - A^*_{0R}A_{\perp R}|}{|A^*_{0L}A_{\|L} + A_{0R}A^*_{\|R}|}, \tag{15}$$

$$F_{\mathrm{L}} = \frac{|A_0|^2}{\Gamma'}, \tag{16}$$

where,

$$A_i A^*_j \equiv A_{iL}(q^2)A^*_{jL}(q^2) + A_{iR}(q^2)A^*_{jR}(q^2) \quad (i,j = 0, \|, \perp), \tag{17}$$

and,

$$\Gamma' = \frac{\mathrm{d}\Gamma}{\mathrm{d}q^2} = \left(|A_{0L}|^2 + |A_{\perp L}|^2 + |A_{\|L}|^2 + (L \to R)\right). \tag{18}$$

[3] These form factors are calculated in the so called *large recoil* limit where the the b and s quarks in the initial and final states are assumed to interact with the spectator quark via the exchange of 'soft' gluons.

The NP sensitivity provided by each of these observables is model and parameter space dependent, however they have been studied for models with non-SM contributions to C_7' in [2, 8, 16]. In the case of $A_{\rm FB}$, it is only the point where the distribution crosses the q^2 axis where the universal form factors cancel at LO, while no such cancellations are found for $F_{\rm L}$. Further theoretical discussions of the observables will be left to Ref. [2] and so we move on to experimental considerations.

III. SENSITIVITY AT LHC*b*

Theoretical treatments of $\overline{B}_d \to \overline{K}^{*0}\mu^+\mu^-$ at NLO normally make use of the QCD factorisation framework [23–25] as described in Ref. [26]. These calculations are involved and no currently available software package allows the simulation of events using the full NLO treatment or the handling of arbitrary NP scenarios from first principles. Instead a toy Monte–Carlo approach can be used where the results of a full calculation, in this case from Ref. [2], are used as input to the model. This allows the generation of toy LHC*b* datasets which can then be used to verify the fitting methods presented in the next sections and access their relative sensitivities.

A. A Toy Model of $\overline{B}_d \to \overline{K}^{*0}\mu^+\mu^-$

A toy Monte–Carlo model of the decay was created within the RooFit framework using Eq. (2) as a probability density function (PDF). The function $I(q^2, \theta_l, \theta_K, \phi)$ is parameterised in terms of the real and imaginary parts of the spin amplitudes, $A_{\perp L,R}$, $A_{\parallel L,R}$, and $A_{0L,R}$, giving twelve parameters. The symmetry relations introduced in Sec. II B can be exploited to reduce the number of free parameters in the system. Eq. (7) is used to make A_{0L} real by setting $\phi_L = -\arg(A_{0L})$ and similarly for A_{0R} with Eq. (8). Eq. (9) can then be used to remove A_{0R} completely by setting $\theta = \arctan(-A_{0L}/A_{0R})$. This leaves nine free parameters at each point in q^2. One more parameter can be eliminated by recognising that the angular observables are not sensitive to the absolute normalisation which cancels in each case. Sensitivity can be gained to the relative normalisation, Γ', by performing an explicit normalisation at some fixed value of q^2, here denoted X_0. We choose to divide all spin amplitudes by the value of $\mathrm{Re}(A_{0L})$ at $X_0 = 3.5\,\mathrm{GeV}^2/c^4$. This leaves the eight degrees of

freedom as expected from inspection of Eq. 6.

Following Ref. [27], the signal is assumed to have a Gaussian distribution in m_B with a width of $14\,\mathrm{MeV}/c^2$ in a window of $m_B \pm 50\,\mathrm{MeV}/c^2$ and a Breit-Wigner in $m_{K\pi}$ with width $48\,\mathrm{MeV}/c^2$ in a window of $m_{K^{*0}} \pm 100\,\mathrm{MeV}/c^2$. A simplified background model is included. This is flat in all angles, effectively treating all background as combinatorial, but follows the q^2 distribution of the signal. Acceptance and *CP* violation effects are neglected allowing us to treat $\overline{B}_d \to \overline{K}^{*0}\mu^+\mu^-$ and its charge conjugate simultaneously. Contributions from non–resonant $\overline{B}_d \to K^-\pi^+\mu^+\mu^-$ events are not included.

B. Generation of Toy Data

The model described in the last section allows the probability of a particular set of observables (θ_l, θ_K, ϕ and q^2) occurring to be calculated. An accept–reject algorithm can then be used to generate a dataset of events with the correct distributions. The q^2 dependence of the PDF is included by generating many sub–datasets in $0.05\,\mathrm{GeV}^2/c^4$ q^2 bins and then combining them, so avoiding the q^2 parameterisation introduced in the next section. In each subbin, Γ' weighted mean spin amplitudes, found using values taken from Ref. [2], were used when calculating $I(q^2, \theta_l, \theta_K, \phi)$. The number of events for a given q^2 subbin is

$$n_{s,b} = N_0^{s,b} \frac{\int_{q_{\min}}^{q_{\max}} \Gamma'}{\int_{4\,\mathrm{m}_\mu^2}^{9\,\mathrm{GeV}^2/c^4} \Gamma'} \,, \tag{19}$$

where N_0^s is the number of signal events expected in $2\,\mathrm{fb}^{-1}$ from [9] and Γ' is derived from the input amplitude calculation. The number of background events was calculated in the same way with the value of N_0^b taken from the same full simulation study. In both cases the value of $n_{s,b}$ is Poisson fluctuated so that not all toy datasets are of the same size. For 10 and $100\,\mathrm{fb}^{-1}$ samples N_0^s and N_0^s were scaled linearly. NP models were dealt with by supplying input spin amplitude values, again from [2], for a particular NP model.

C. Fitting of Data to Extract Sensitivities

As discussed in Sec. III A, the decay PDF has eight unconstrained spin amplitudes which can be extracted from data using a fit. The q^2 dependence of these amplitudes must be taken into account. We can explicitly parameterise this dependence or divide the experimental

data into q^2 bins and perform an independent fit in each bin, making the assumption that the q^2 dependence can be neglected. The latter approach allows for fewer parameters to be used, but produces significant systematic fit biases if the q^2 dependence across the bin is non–linear and the effect ignored. These biases arise from the differing q^2 dependence of each of the spin amplitude components and appear even if the fit is properly convergent[4]. It was found that the biases could not be eliminated while preserving enough statistics in each bin to perform the fit reliably. Instead an unbinned approach was used where the q^2 dependence of each spin amplitude component is parameterised as a $2^{\rm nd}$ order polynomial, the coefficients of which are then extracted.

The parameterisation is as follows. For $\mathrm{Re}(A_{0L})$ we use a standard polynomial

$$f_p(q^2) = A_p(q^2 - X_0)^2 + B_p(q^2 - X_0) + C_p, \tag{20}$$

while for the other amplitude components we use a Chebyshev polynomial,

$$f_c(q^2) = A_c(2(q^2 - X_0)^2 - 1) + B_c(q^2 - X_0) + C_c. \tag{21}$$

In this parameterisation $f_c^{\mathrm{Re}(A_{0R})} = f_c^{\mathrm{Im}(A_{0L})} = f_c^{\mathrm{Im}(A_{0R})} = 0$ and $C_p^{\mathrm{Re}(A_{0L})} = 1$ once the symmetry transforms and normalisation, introduced in Sec. III A, have been applied. Making a measurement in this framework requires that the polynomial ansatz be satisfied for all spin amplitude components in the range $q^2_{\rm min} - q^2_{\rm max}$. This was verified for the five physics models considered in Ref. [2], but clearly introduces a weak source of model dependence. Fig. 11 of Appendix B shows an example dataset, generated following Sec. III B, where numerical projections of the final polynomial PDF for each of the experimental observables can be seen. The background component is also shown separately. The agreement between the binned generation PDF and the unbinned fitting PDF can be seen to be excellent.

By generating an ensemble of toy–LHCb datasets and then fitting them with the polynomial model, the experimental sensitivities for a given integrated luminosity can be estimated and any biases introduced by the method can be found. The fit was well behaved but could be sensitive to the initial values chosen for the fit parameters. To deal with this, the fit was run repeatedly with randomly chosen initial values until an accurate covariance matrix was

[4] If it was possible to integrate Eq. (2) over q^2 then these problems could be avoided. However it is not possible to do this in a model independent way as the q^2 dependence of the spin amplitudes must be explicitly known.

found[5]. Each refit was initialised from scratch so that each refit result was independent of the last. For an ensemble of 1076 $10\,\text{fb}^{-1}$ experiments, each of which assumed the SM, the mean number of refits required was 2.97, and the maximum was 103. For 1006 $2\,\text{fb}^{-1}$ SM datasets the mean increased to 6.81 and 0.7% of experiments failed to converge at all[6]. It was verified that the final fit results were independent of the starting values by performing several refits of each dataset. Any variation on the output of repeated successful refits was seen to be small compared to the errors on the fit parameters.

There were significant correlations between parameters in some of the experiments. The constant terms of $\text{Re}(A_{\parallel R})$ and $\text{Re}(A_{\perp R})$ and to a lesser extent those of $\text{Im}(A_{\parallel R})$ and $\text{Im}(A_{\perp R})$ were anti–correlated, leading to significant biases on these parameters. The biases were not seen in the angular observables, as the correlations meant that they cancelled out, but can be seen in the individual amplitude components shown in Appendix A. These correlations also seem not to affect the angular distribution, which is well reproduced by the fit, as shown in Appendix B for a randomly chosen toy experiment.

IV. RESULTS

The methods described in Sec. III were used to generate and fit ensembles of experiments for three different LHCb integrated luminosities, 2, 10 and $100\,\text{fb}^{-1}$. These are the expected dataset sizes for a nominal year of data–taking, at the end of LHCb data–taking and at the end of a run with an upgraded SuperLHCb detector respectively. The results for $10\,\text{fb}^{-1}$ will be presented here, while those for the other integrated luminosities are available in Appendix C.

Fig. 3(a) shows the experimental sensitivity to A_{FB} in the SM as derived from the ensemble of $10\,\text{fb}^{-1}$ experiments. The median value is shown as the solid (red) line while the light and dark (blue) regions mark the contours of 1 and 2 σ significance at their external boundaries. These are calculated by ordering the ensemble of results and then selecting 33% and 47.5% of experiments either side of the median at any given q^2 value.

[5] Signified by a `Minuit` covariance quality of three.

[6] The maximum number of allowed refits was fixed at 1600 in order to limit the amount of Grid resources used. This number could be dramatically increased if required when the real measurement was made.

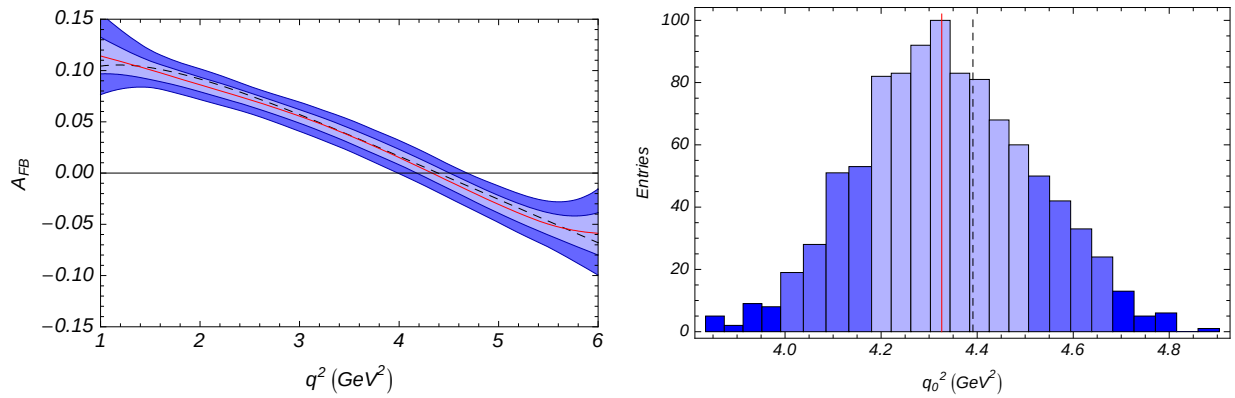

(a) $A_{\rm FB}$ (b) $A_{\rm FB}$ zero–crossing

FIG. 3: (a) The estimated experimental sensitivity to $A_{\rm FB}$ as a function of q^2 for a $10\,{\rm fb}^{-1}$ sample of LHCb data, assuming the SM. The dashed (black) line is the SM input distribution. The solid (red) line shows the median result over an ensemble of a thousand toy experiments, while the light and dark bands show the 1σ and 2σ confidence levels. (b) The ensemble of $A_{\rm FB}$ zero–crossing points found from each experiment, giving an estimated value of $4.33^{+0.18}_{-0.16}\,{\rm GeV}^2/c^4$. The colour scheme is the same as in (a), but zero–crossings outside the 95% confidence are also shown in the outer (dark blue) regions.

Fig. 3(b) shows explicitly the ensemble of $A_{\rm FB}$ zero–crossing point results[7]. By comparing the dashed (black) SM and median lines in both figures, the agreement between input and output distributions can be seen. The fit fails to reproduce the input exactly, but the discrepancy is small compared to the overall experimental uncertainty. These discrepancies seem to be due to the failure of the polynomial ansatz, and are particularly significant at the edges of the q^2 region under consideration as seen by the deviation of the solid red (input) and dashed black (median fit result) lines in the figure.

Figs. 4(a) and 4(b) show the sensitivity bands for the new observables $A_T^{(3)}$ and $A_T^{(4)}$. The limitations of the polynomial ansatz can again be seen, but the overall shape is well reproduced, and the deviation is small compared to the statistical errors. Figs. 5(a), 5(b) and 5(c) show respectively the sensitivity bands for $A_{\rm Im}$, $A_T^{(2)}$ and $F_{\rm L}$. Like $A_{\rm FB}$, these observables

[7] One of the thousand toy experiments did not have a zero–crossing point and so is excluded from the distribution.

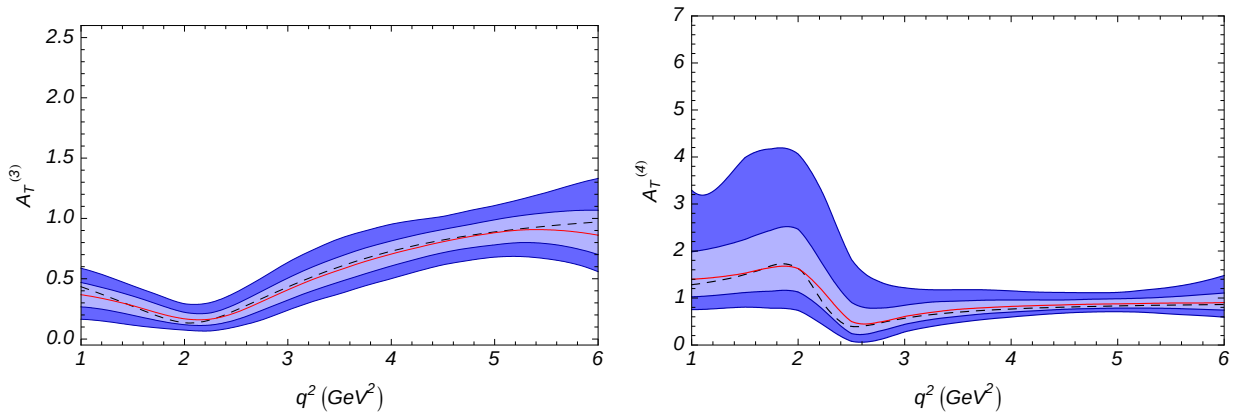

(a) $A_T^{(3)}$ (b) $A_T^{(4)}$

FIG. 4: Estimated experimental sensitivities to (a) $A_T^{(3)}$ and (b) $A_T^{(4)}$ as a function of q^2 for $10\,\text{fb}^{-1}$ of LHCb data assuming the SM. The colour scheme is the same as in Fig. 3.

are also accessible by making projection fits as discussed in Sec. V. Finally Fig. 5(d) shows the sensitivity band for Γ' relative to the point $X_0 = 3.5\,\text{GeV}^2/c^4$, the midpoint of the q^2 range.

V. COMPARISON WITH A SIMULTANEOUS PROJECTION FIT

A. A_{FB}, A_{Im}, $A_T^{(2)}$ and F_{L}

In Ref. [27], angular projections over Eq. (2) were used to extract the parameters A_{FB}, A_{Im}, $A_T^{(2)}$ and F_{L} in bins of q^2. For the $\overline{B}_d$ decay:

$$\frac{d\Gamma'}{d\phi} = \frac{\Gamma'}{2\pi}\left(1 + \frac{1}{2}(1 - F_{\text{L}})A_T^{(2)}\cos 2\phi + A_{\text{Im}}\sin 2\phi\right) \tag{22a}$$

$$\frac{d\Gamma'}{d\theta_l} = \Gamma'\left(\frac{3}{4}F_{\text{L}}\sin^2\theta_l + \frac{3}{8}(1 - F_{\text{L}})(1 + \cos^2\theta_l) + A_{\text{FB}}\cos\theta_l\right)\sin\theta_l \tag{22b}$$

$$\frac{d\Gamma'}{d\theta_K} = \frac{3\Gamma'}{4}\sin\theta_k\left(2F_{\text{L}}\cos^2\theta_K + (1 - F_{\text{L}})\sin^2\theta_K\right) \tag{22c}$$

These differential widths were used as PDFs in the construction of three new RooFit models with the same physics and background treatment as that described in Sec. III A. Simultaneous fits to the three decay angles were performed in single bins of q^2 from $1 - 6\,\text{GeV}^2/c^4$ to find rate weighted averages of each observable across the bin. Input datasets were gen-

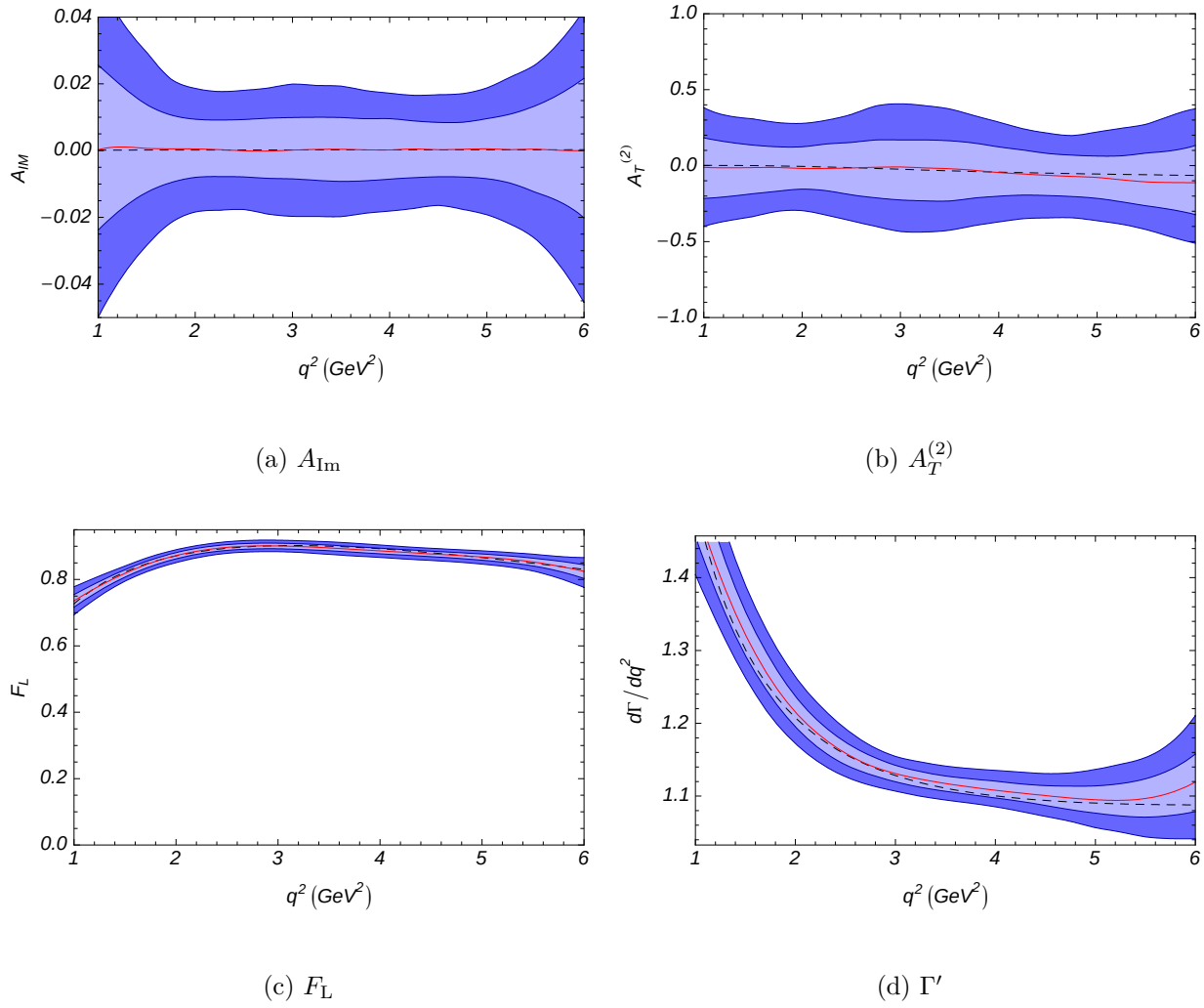

(a) $A_{\rm Im}$ (b) $A_T^{(2)}$

(c) $F_{\rm L}$ (d) Γ'

FIG. 5: Estimated experimental sensitivities to (a) $A_{\rm Im}$, (b) $A_T^{(2)}$, (c) $F_{\rm L}$ and (d) Γ', as a function of q^2 for $10\,{\rm fb}^{-1}$ of LHCb data assuming the SM. The colour scheme is the same as in Fig. 3.

erated as in Sec. III B. A reasonable comparison can be made between the full angular and projection fit approaches by explicitly calculating the rate average over the q^2 range for each observable, A, using

$$\langle A\rangle = \frac{\int_{q^2_{\rm min}}^{q^2_{\rm max}} \frac{{\rm d}\Gamma}{{\rm d}q^2} A(q^2)}{\int_{q^2_{\rm min}}^{q^2_{\rm max}} \frac{{\rm d}\Gamma}{{\rm d}q^2}}, \tag{23}$$

where ${\rm d}\Gamma/{\rm d}q^2$ is extracted directly from the fit, as shown in Fig. 5(d).

In Tab. 6 resolution estimates from an ensemble of a thousand fits are shown for both full angular and projection fits. It can be seen that the full angular approach provides a significant increase in experimental resolution for all observables considered. The difference

	Input	Projection		Full Angular		$\frac{(\hat{\sigma}_{\rm F}-\sigma_{\rm P})}{\sigma_{\rm P}}$
	$\langle A\rangle_{\rm I}$	$\langle A\rangle_{\rm P}$	$\sigma_{\rm P}$	$\langle A\rangle_{\rm F}$	$\sigma_{\rm F}$	%
$A_{\rm FB}$	0.036	0.0325	$\pm$0.0078	0.0344	$^{+0.0047}_{-0.0050}$	38
$A_{\rm Im}$	0.000	0.000	$\pm$0.015	0.0004	$^{+0.0060}_{-0.0057}$	61
$A_T^{(2)}$	-0.030	-0.03	$\pm$0.26	-0.043	$^{+0.095}_{-0.094}$	64
$F_{\rm L}$	0.865	0.8799	$\pm$0.0064	0.8582	$^{+0.0052}_{-0.0058}$	14

FIG. 6: Comparison between integrated values for the angular observables $A_{\rm FB}$, $A_{\rm Im}$, $A_T^{(2)}$ and $F_{\rm L}$ in the range $1 \leq q^2 \leq 6\,{\rm GeV}^2/c^4$ from an ensemble of a thousand $10\,{\rm fb}^{-1}$ LHCb datasets with averaged input values $\langle A\rangle_{\rm I}$. $\langle A\rangle_{\rm P,F}$ are the median values of the averages as calculated using Eq. (23), while $\sigma_{\rm P,F}$ are estimates of the 1σ uncertainty for both methods. The percentage resolution improvement offered by the full angular analysis relative to the projection fit method is shown in the last column, where $\hat{\sigma}_{\rm F}$ is the mean of the asymmetric uncertainties for each observable.

in resolutions between the full angular and projection fit approaches, shown in the table, is particularly significant for $A_T^{(2)}$. This arises from the $(1 - F_{\rm L})$ suppression in Eq. (22a) where $F_{\rm L} \approx 0.87$ in the SM. In contrast, $F_{\rm L}$ is well constrained in the projections and the full angular fits do not significantly improve the resolutions attainable.

B. The $A_{\rm FB}$ zero–crossing Point

A comparison of the sensitivity to the $A_{\rm FB}$ zero–crossing point can also be found by following the methods of Ref. [28], but fitting the three angles simultaneously. In this case a thousand $10\,{\rm fb}^{-1}$ datasets were binned into five q^2 bins in the range $1 \leq q^2 \leq 6\,{\rm GeV}^2/c^4$, each with width of $1\,{\rm GeV}^2/c^4$. For each dataset an independent simultaneous projection fit was performed in each of the q^2 bins and the resulting points fit to a straight line in the range $2 \leq q^2 \leq 6\,{\rm GeV}^2/c^4$ to extract the zero–crossing point. An example of this is shown in Fig. 7. The median zero–crossing found was $4.35^{+0.23}_{-0.24}\,{\rm GeV}^2/c^4$ for an input value of $4.39\,{\rm GeV}^2/c^4$. The quoted sensitivity is in reasonable agreement with that found in Ref. [28], although the two results are not directly comparable. Comparing now with the full angular fit, we see a 28% improvement in the resolution relative to the projections result.

The value of $A_{\rm FB}$ at a given q^2 value is a quadratic function of the universal form factor

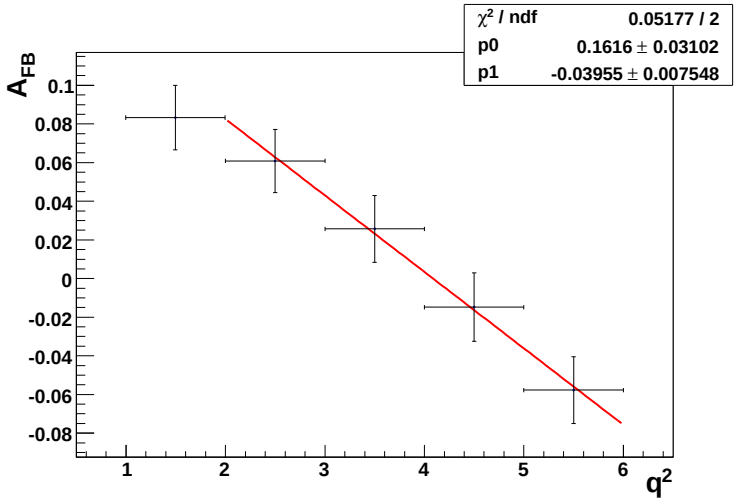

FIG. 7: An example toy experiment in which an $A_{\rm FB}$ value has been extracted in five independent $1\,{\rm GeV}^2/c^4$ q^2 bins using a simultaneous projection fit to the three decay angles. The points show the $A_{\rm FB}$ value found for each q^2 bin and its error. The x error bar shows the width of the q^2 bin. The solid (red) line shows a fit to the linear function $y = p1\,x + p0$ in the range $2 \leq q^2 \leq 6\,{\rm GeV}^2/c^4$ as used in [28]. This allows a zero–crossing point of $q_0^2 = 4.09 \pm 0.21\,{\rm GeV}^2/c^4$ to be extracted for this particular experiment.

$\zeta_\perp$ [26], introduced in Sec. II C. Again, following [26], the energy dependence of the form factor can be parameterised as

$$\zeta_\perp(q^2) = \zeta_\perp(0)\left(\frac{1}{1 - q^2/M_B^2}\right)^2, \tag{24}$$

where M_B is the mass of the $\overline{B}_d$ and $\zeta_\perp(0)$ gives the normalisation at $q^2 = 0$. This can be extracted from experiment by performing a fit to $\overline{B}_d \to \overline{K}^{*0}\gamma$ measurements or from QCD factorisation [26, 29]. At the zero–crossing point, these form–factors cancel at LO, however the *particular* value of $\zeta_\perp(0)$ used to generate the $A_{\rm FB}$ spectrum will affect the gradient of $A_{\rm FB}$ going through the zero–crossing point quadratically.

The experimental sensitivity for the zero–crossing point should be an approximately linear function of the $A_{\rm FB}$ gradient, so the value of $\zeta_\perp(0)$, both in our studies and in nature, strongly affects the experimental sensitivity to the zero–crossing point. The zero–crossing sensitivities we quote are extracted from toy input data where $\zeta_\perp(0) = 0.26$, based on the updated value from [30]. This should be contrasted with the model used in [28] and based upon [5], which uses a value of $\zeta_\perp(0) = 0.34$. If this value had instead been used in our study

then an improvement in the zero–crossing resolution by a factor two would be expected. The observables $A_T^{(2-4)}$ are constructed to have no sensitivity to the form factors over the complete q^2 range under study and so no major change in their resolutions is expected as we vary $\zeta_\perp(0)$.

VI. NEW PHYSICS MODEL DISCRIMINATION

In this section the methods in Sec. III will be applied to a generic NP model with right–handed currents in order to demonstrate the discriminating power of the angular observables. Sensitivities to the observables introduced in Sec. II C are extracted and compared to the SM theoretical distributions.

The NP model to be examined, SUSY–b, is a non–minimal flavour changing version of the MSSM with R–parity conservation, where the gluino mass is large, $m_{\tilde{g}} = 1\,\text{TeV}$, the down squark mass is $m_{\tilde{d}} = 250\,\text{GeV}$ and there is a low value of $\tan\beta = 5$ [8]. In addition, there is a single insertion in the down squark mass matrix, parameterised by $(\delta^d_{LR})_{32} = 0.036$, which generates right–handed currents. The flavour diagonal parameters are fixed at $\mu = M_1 = M_2 = M_{H^+} = m_{\tilde{u}} = 1\,\text{TeV}$. It has been recently re–verified that this scenario is within current experimental and theoretical bounds [2].

This model has been chosen as it generates non–SM values of C_7'; $(C_7, C_7') = (-0.32, 0.24)$ which should be compared with the SM values of $(-0.31, 0.00)$. The observables A_{Im}, A_{FB} (and its zero–crossing) and F_{L} are not very sensitive to deviations in C_7' and so offer little discrimination power. However, $A_T^{(2)}$, $A_T^{(3)}$ and $A_T^{(4)}$ have been constructed in such as way as to maximise the sensitivity to this Wilson coefficient and hence allow better discrimination between SUSY–b and the SM.

Fig. 8 shows the comparison between the estimated sensitivities to SUSY–b, as extracted from an ensemble of a thousand $10\,\text{fb}^{-1}$ LHCb datasets and the SM theoretical distribution from Ref. [2] for $A_T^{(2)}$, $A_T^{(3)}$, $A_T^{(4)}$. The power of these observables is clear for observing non–SM values of C_7', particularly in the low q^2 region where the operator $\mathcal{O}_7^{(\prime)}$ dominates. Due to the correlations along the band for both the theory and experimental curves, careful thought is needed to turn these measurements into a confidence level that the SM could be rejected if indeed nature turned out to be supersymmetric in the way modelled by SUSY–b. However, it seems clear that such a measurement could be of great interest if NP is discovered at the

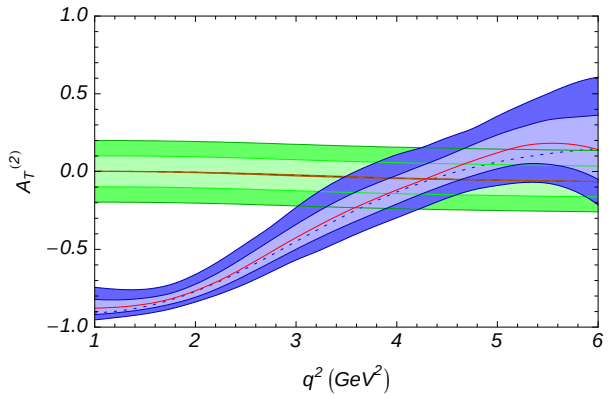

(a) $A_T^{(2)}$

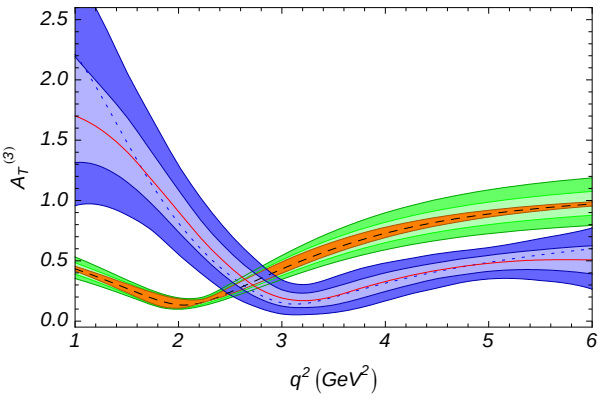

(b) $A_T^{(3)}$

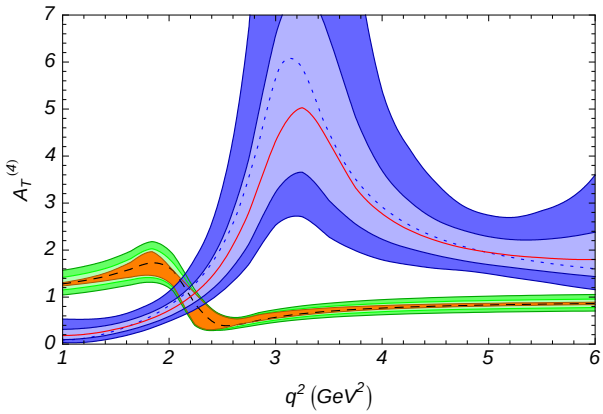

(c) $A_T^{(4)}$

FIG. 8: Comparison between the estimated experimental sensitivities to $A_T^{(2)}$, $A_T^{(3)}$, $A_T^{(4)}$ and the theoretical SM distribution. The solid (red) line shows the median of values extracted from an ensemble of a thousand 10 fb^{-1} LHCb datasets where SUSY–b was used as the input model, shown as the (dark blue) dotted line. The (light and dark blue) bands either side of the median show asymmetric 1 and 2 σ confidence levels as in Fig. 3. The SM theory bands are explained in more detail in Ref. [2]. The dashed (black) line is the SM central value, while the surrounding bands (orange, light green, dark green), are respectively the theoretical uncertainties excluding $\mathcal{O}(\Lambda/m_b)$ corrections, and those including 5% and 10% Λ/m_b corrections.

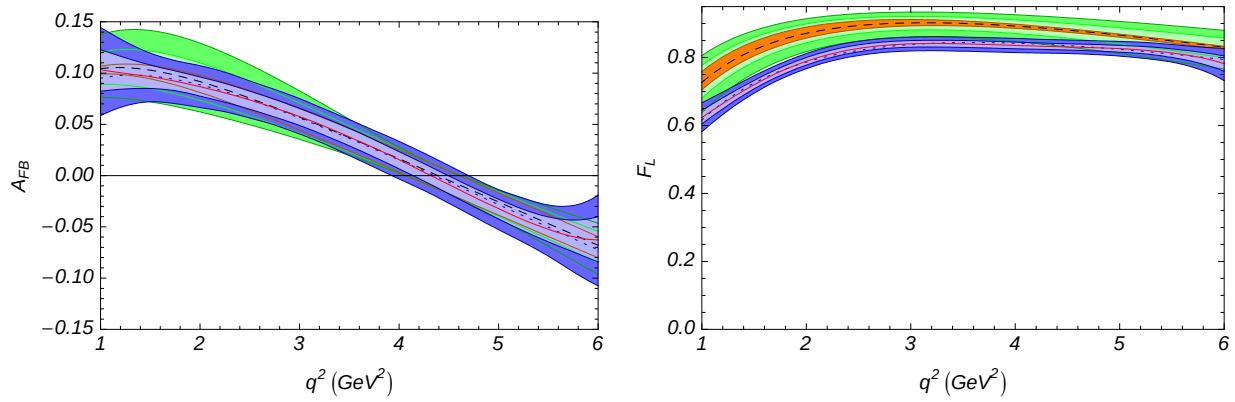

(a) $A_{\rm FB}$ (b) $F_{\rm L}$

FIG. 9: Comparison between the estimated experimental sensitivities to $A_{\rm FB}$ and $F_{\rm L}$ and the theoretical SM distribution. The colour scheme used is the same as in Fig. 8.

LHC.

Fig. 9 shows the same comparison for the angular observables $A_{\rm FB}$ and $F_{\rm L}$. As expected, these observables offer poor sensitivity to C_7' across the entire q^2 range. $F_{\rm L}$ looks more promising than $A_{\rm FB}$ for this particular NP scenario, but is hindered by the large theoretical uncertainties on the SM prediction.

VII. SUMMARY AND OUTLOOK

The full angular fit for $\overline{B}_d \to \overline{K}^{*0}\mu^+\mu^-$ allows access to any arbitrary combination of the spin amplitudes as a function of q^2 in the region $1 \leq q^2 \leq 6\,{\rm GeV}^2/c^4$. A set of angular observables can be constructed from these amplitudes which give LHCb great power to discover NP and to discriminate between models in a model independent way. In this note, several of these observables have been studied in order to estimate the experimental sensitivities at LHCb for 2, 10 and $100\,{\rm fb}^{-1}$ datasets. It was seen that the method could be applied successfully in a simplified Monte–Carlo treatment for even the smallest of these datasets, and that for larger integrated luminosities, these observables offer powerful discrimination in the case where $C_7' \neq C_{7\,\rm SM}'$.

Putting these methods into practise at LHCb will be a great technical challenge, and the success of the analysis will depend on our ability to understand the detector acceptance and

the angular shapes of our backgrounds. This note has demonstrated that the sensitivity gained by performing the full angular analysis makes this a very interesting measurement to make at LHCb, and one that could potentially be done after a few years of stable running.

Acknowledgments

The work presented in this note was done in collaboration with T. Hurth, J. Matias and M. Ramon, and would not have been possible without their input.

APPENDIX A: SENSITIVITIES TO AMPLITUDE COMPONENTS

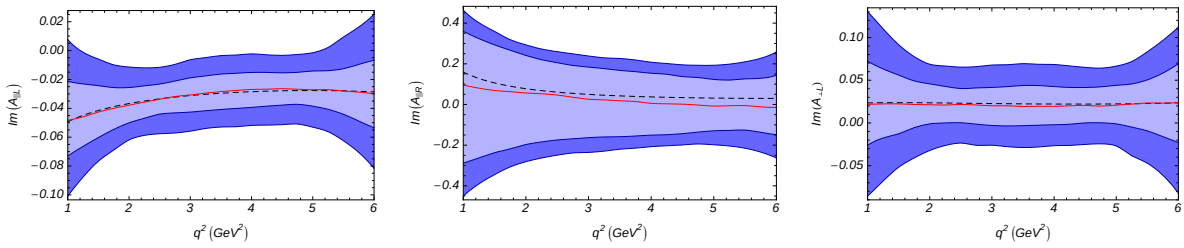

(a) $\mathrm{Im}(A_{\parallel L})$ (b) $\mathrm{Im}(A_{\parallel R})$ (c) $\mathrm{Im}(A_{\perp L})$

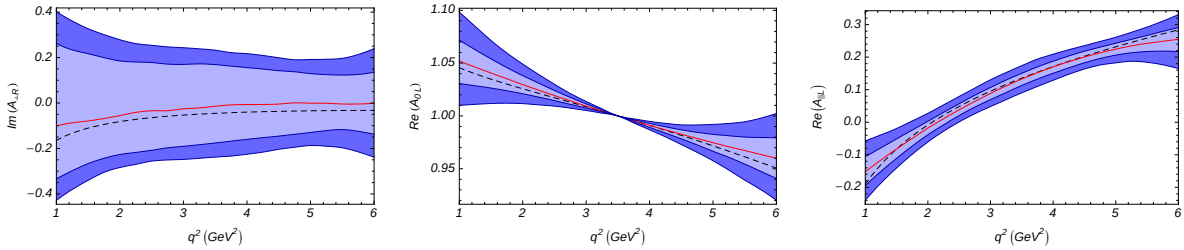

(d) $\mathrm{Im}(A_{\perp R})$ (e) $\mathrm{Re}(A_{0L})$ (f) $\mathrm{Re}(A_{\parallel L})$

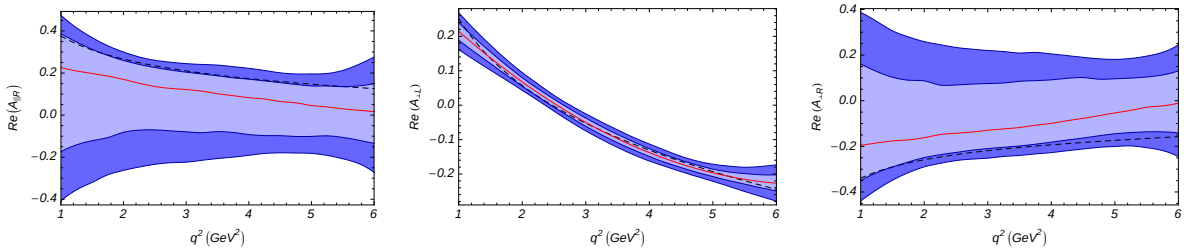

(g) $\mathrm{Re}(A_{\parallel R})$ (h) $\mathrm{Re}(A_{\perp L})$ (i) $\mathrm{Re}(A_{\perp R})$

FIG. 10: Sensitivity bands for the individual spin amplitude components as a function of q^2 for $10\,\mathrm{fb}^{-1}$ of SM data. The colour scheme is the same as in Fig. 3. The effect of the normalisation at $q^2 = X_0 = 3.5\,\mathrm{GeV}^2/c^4$ can be seen on $\mathrm{Re}(A_{0L})$, as can the strong anti–correlation between $\mathrm{Re}(A_{\parallel R})$ and $\mathrm{Re}(A_{\perp R})$.

APPENDIX B: ANGULAR PROJECTIONS AND FIT QUALITY

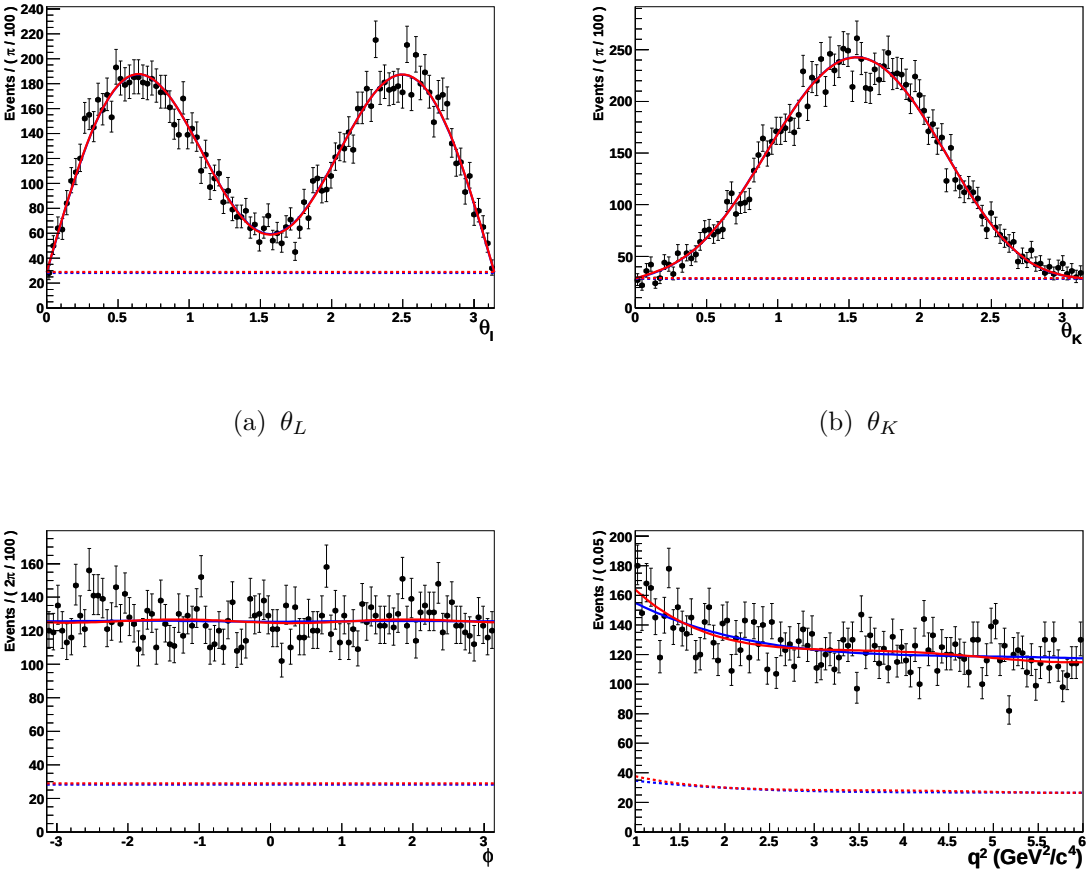

(a) θ_L (b) θ_K

(c) ϕ (d) q^2

FIG. 11: Numerical projections of the full polynomial fit PDF over an example toy dataset for each of the experimental observables. The points show a randomly chosen $10\,\mathrm{fb}^{-1}$ dataset, generated assuming the SM as described in Sec. III B. The solid red line shows numerical projections over this dataset with the full angular polynomial PDF, described in Sec. III A, with its parameters set via a fit to the dataset. The dashed line shows only the background contribution. Underlayed on each plot is the blue line showing the input PDF. The parameters of this PDF have been set by performing a polynomial fit to each of the K^{*0} spin amplitudes. Comparing these two lines we see that the full angular fit is able to extract the PDF parameters with good accuracy. The differences are largest for the q^2 distribution.

APPENDIX C: RESULTS FOR 2 AND 100 fb^{-1}

1. 2 fb^{-1}

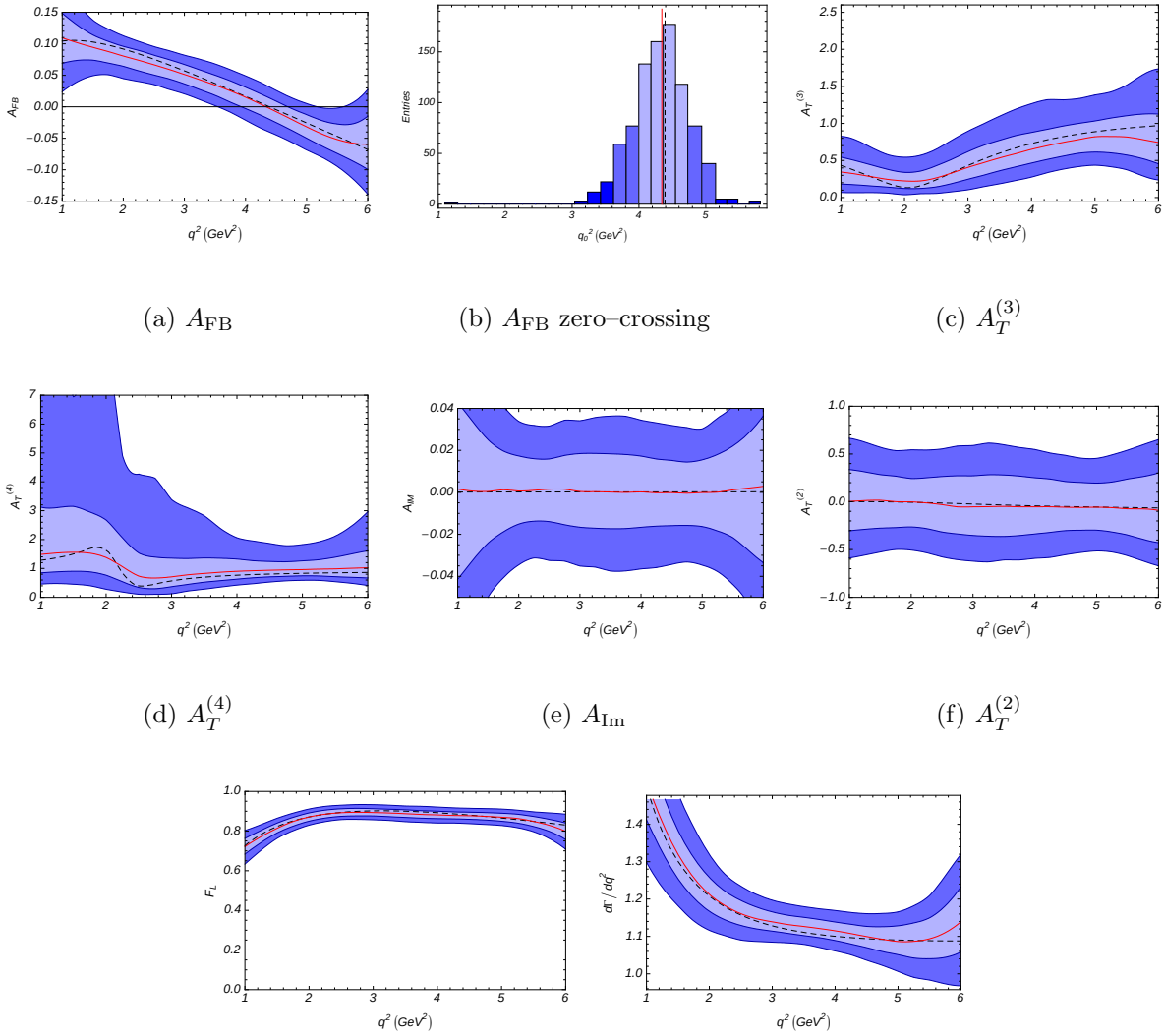

(a) A_{FB} (b) A_{FB} zero–crossing (c) $A_T^{(3)}$

(d) $A_T^{(4)}$ (e) A_{Im} (f) $A_T^{(2)}$

(g) F_{L} (h) Γ'

FIG. 12: Estimated experimental sensitivities for $2\,\mathrm{fb}^{-1}$ of LHCb data assuming the SM. The zero–crossing point extracted from (b) is $4.34^{+0.39}_{-0.34}\,\mathrm{GeV}^2/c^4$. The colour scheme is the same as in Fig. 3.

2. 100 fb^{-1}

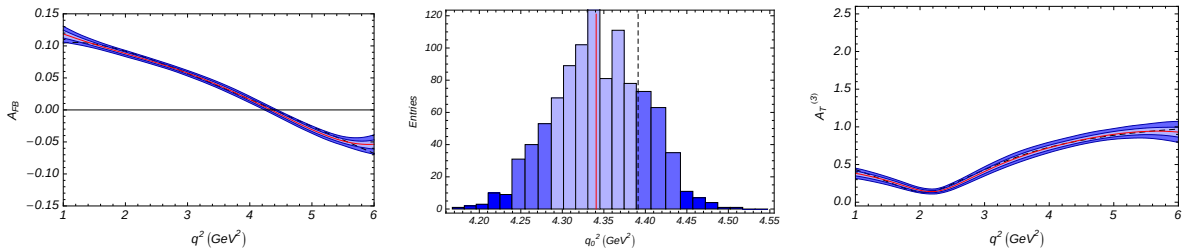

(a) $A_{\rm FB}$ (b) $A_{\rm FB}$ zero–crossing (c) $A_T^{(3)}$

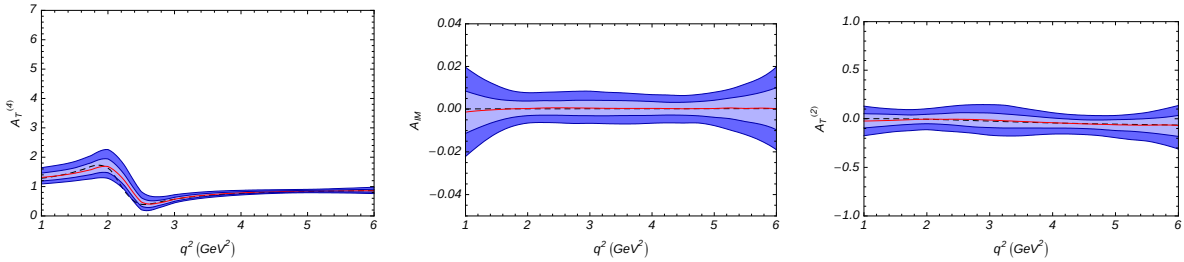

(d) $A_T^{(4)}$ (e) $A_{\rm Im}$ (f) $A_T^{(2)}$

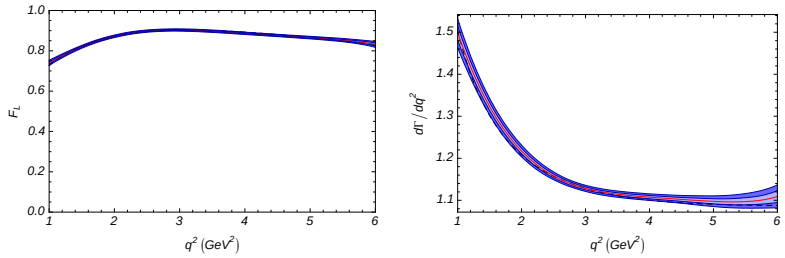

(g) $F_{\rm L}$ (h) Γ'

FIG. 13: Estimated experimental sensitivities for 100 fb^{-1} of LHCb data assuming the SM. The zero–crossing point extracted from (b) is $4.34^{+0.054}_{-0.048}$ GeV$^2/c^4$; the bias on its value is now significant and could perhaps be improved by increasing the order of the polynomials used in the full angular fit. The colour scheme is the same as in Fig. 3.

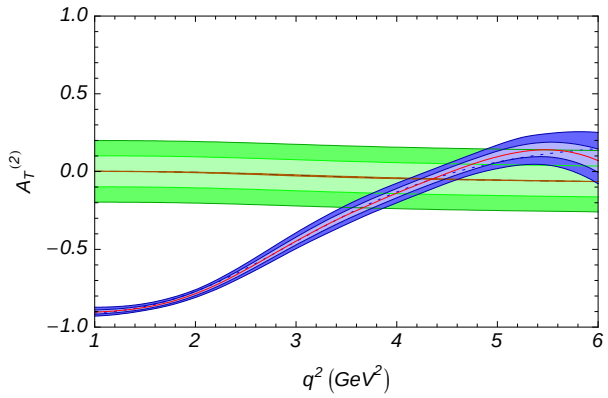

(a) $A_T^{(2)}$

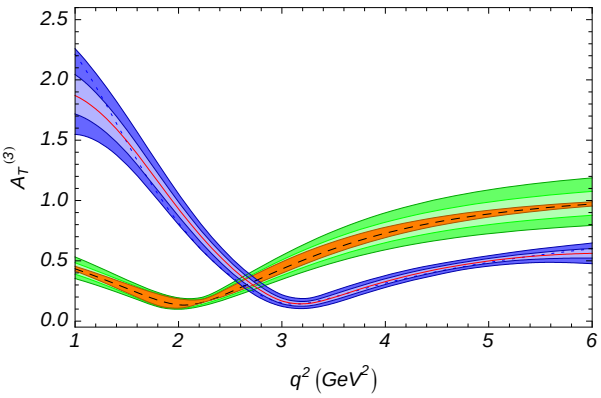

(b) $A_T^{(3)}$

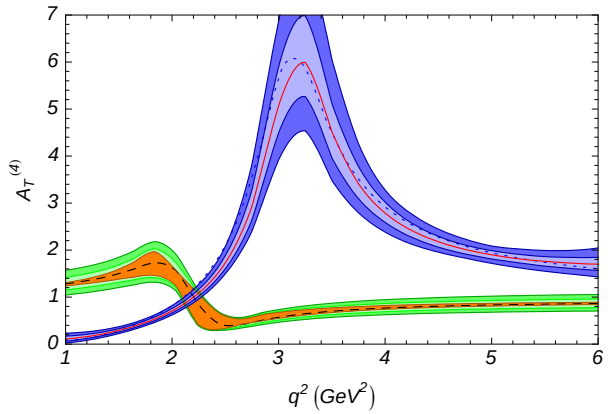

(c) $A_T^{(4)}$

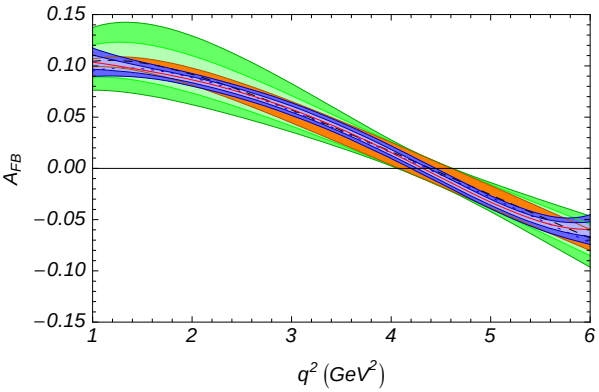

(d) $A_{\rm FB}$

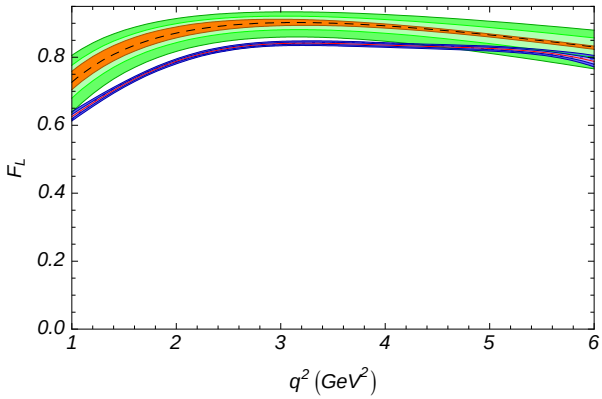

(e) $F_{\rm L}$

FIG. 14: Comparison between the estimated experimental sensitivities to $A_T^{(2)}$, $A_T^{(3)}$, $A_T^{(4)}$, $A_{\rm FB}$ and $F_{\rm L}$ and the theoretical SM distribution for $100\,{\rm fb}^{-1}$ of LHCb data assuming the SUSY–b scenario. The colour scheme is the same as in Fig. 8.

[1] T. Hurth, Int. J. Mod. Phys. **A22**, 1781 (2007), arXiv:hep-ph/0703226.

[2] U. Egede, T. Hurth, J. Matias, M. Ramon, and W. Reece, JHEP **11**, 032 (2008), arXiv:hep-ph/0807.2589.

[3] A. Ishikawa et al. (Belle), Phys. Rev. Lett. **91**, 261601 (2003), arXiv:hep-ex/0308044.

[4] C. Amsler et al. (Particle Data Group), Phys. Lett. **B667**, 1 (2008).

[5] A. Ali, P. Ball, L. T. Handoko, and G. Hiller, Phys. Rev. **D61**, 074024 (2000), arXiv:hep-ph/9910221.

[6] C. Bobeth, T. Ewerth, F. Kruger, and J. Urban, Phys. Rev. **D64**, 074014 (2001), arXiv:hep-ph/0104284.

[7] P. Colangelo, F. De Fazio, R. Ferrandes, and T. N. Pham, Phys. Rev. **D73**, 115006 (2006), arXiv:hep-ph/0604029.

[8] E. Lunghi and J. Matias, JHEP **04**, 058 (2007), arXiv:hep-ph/0612166.

[9] J. Dickens, V. Gibson, C. Lazzeroni, and M. Patel (2007), CERN-LHCb-2007-038.

[10] B. Aubert et al. (*BABAR*), Phys. Rev. **D73**, 092001 (2006), arXiv:hep-ex/0604007.

[11] A. Ishikawa et al. (Belle), Phys. Rev. Lett. **96**, 251801 (2006), arXiv:hep-ex/0603018.

[12] B. Aubert et al. (*BABAR*) (2008), arXiv:hep-ex/0804.4412.

[13] B. Aubert et al. (*BABAR*) (2008), arXiv:hep-ex/0807.4119.

[14] I. Adachi et al. (Belle) (2008), arXiv:hep-ex/0810.0335.

[15] B. Grinstein and D. Pirjol, Phys. Rev. **D73**, 094027 (2006), arXiv:hep-ph/0505155.

[16] F. Kruger and J. Matias, Phys. Rev. **D71**, 094009 (2005), arXiv:hep-ph/0502060.

[17] G. Hiller and F. Kruger, Phys. Rev. **D69**, 074020 (2004), arXiv:hep-ph/0310219.

[18] W. Altmannshofer et al. (2008), arXiv:hep-ph/0811.1214.

[19] J. Charles, A. Le Yaouanc, L. Oliver, O. Pene, and J. C. Raynal, Phys. Rev. **D60**, 014001 (1999), arXiv:hep-ph/9812358.

[20] J. Charles, A. Le Yaouanc, L. Oliver, O. Pene, and J. C. Raynal, Phys. Lett. **B451**, 187 (1999), arXiv:hep-ph/9901378.

[21] M. J. Dugan and B. Grinstein, Phys. Lett. **B255**, 583 (1991).

[22] M. Beneke and T. Feldmann, Nucl. Phys. **B592**, 3 (2001), arXiv:hep-ph/0008255.

[23] C. W. Bauer, S. Fleming, D. Pirjol, and I. W. Stewart, Phys. Rev. **D63**, 114020 (2001),

arXiv:hep-ph/0011336.

[24] C. W. Bauer, D. Pirjol, and I. W. Stewart, Phys. Rev. **D65**, 054022 (2002), arXiv:hep-ph/0109045.

[25] M. Beneke, A. P. Chapovsky, M. Diehl, and T. Feldmann, Nucl. Phys. **B643**, 431 (2002), arXiv:hep-ph/0206152.

[26] M. Beneke, T. Feldmann, and D. Seidel, Nucl. Phys. **B612**, 25 (2001), arXiv:hep-ph/0106067.

[27] U. Egede (2007), CERN-LHCb-2007-057.

[28] J. Dickens, V. Gibson, C. Lazzeroni, and M. Patel (2007), CERN-LHCb-2007-039.

[29] P. Ball and V. M. Braun, Phys. Rev. **D58**, 094016 (1998), arXiv:hep-ph/9805422.

[30] M. Beneke, T. Feldmann, and D. Seidel, Eur. Phys. J. **C41**, 173 (2005), arXiv:hep-ph/0412400.